

***XMM-Newton* observations of the complex spin pulse of the intermediate polar PQ Geminorum**

P.A. Evans¹*, Coel Hellier¹ and Gavin Ramsay²

¹ *Astrophysics Group, School of Chemistry and Physics, Keele University, Staffordshire, ST5 5BG*

² *Mullard Space Science Laboratory, University College London, Holmbury St. Mary, Dorking, Surrey RH5 6NT*

Accepted Received

ABSTRACT

The intermediate polar PQ Geminorum shows a complex pulsation, caused by a spinning white dwarf, which varies markedly with wavelength. We report *XMM-Newton* observations, including the soft and hard X-ray bands and the first UV lightcurves of this star. We update the ephemeris for PQ Gem allowing us to align these data with a compilation of lightcurves from the optical to the X-ray. Building on work by previous authors, we show how a model in which accretion flows along skewed field lines, viewed at the correct inclination, can explain the major features of the lightcurves in all bands. We discuss how the skew of the field lines relates to the spinning down of the white-dwarf rotation.

Key words: accretion, accretion discs – stars: individual: PQ Gem (RE J0751+14) – novae, cataclysmic variables – X-rays: binaries.

1 INTRODUCTION

PQ Geminorum (RE J0751+14) was discovered in the *ROSAT* Wide Field Camera all-sky survey by Mason et al. (1992). They identified it as an intermediate polar (IP) – a magnetic subclass of the cataclysmic variable stars (see, e.g., Patterson 1994; Hellier 2001 for reviews of this class of star).

The spin-pulse profile of PQ Gem is complex, and thus presents us with many clues as to the accretion geometry. It is one of the few IPs to show polarised light that varies over the spin cycle. It also has a soft blackbody component to its X-ray emission; out of the twenty-five known IPs, to date only six have been shown to have such a component (see, e.g., de Martino et al. 2004). For this reason it has been much studied, both in optical photometry (Hellier, Ramseyer & Jablonski 1994), polarimetry (Piironen, Hakala & Coyne 1993; Potter et al. 1997), spectroscopy (Hellier 1997) and X-rays (e.g. Duck et al. 1994; Mason 1997).

All of these features help us to constrain the geometry of the system. The most recent model (Potter et al. 1997; Mason 1997) suggests that accretion occurs along magnetic field lines which precede the pole, and that these field lines pick up material from outside the corotation radius (i.e. where the orbital motion of the disc is slower than the rotation of the white dwarf). Optical Doppler tomography also shows evidence for accretion along preceding field lines (Hellier

1997). Accreting from outside the corotation radius is likely to produce a braking torque on the white dwarf, and this is consistent with the spin-down reported by Mason (1997).

We report here an analysis of an *XMM-Newton* observation of PQ Gem, aimed at testing the model of Potter et al. (1997) and Mason (1997).

2 OBSERVATIONS AND POWER SPECTRA

PQ Gem was observed for 36 ks by the *XMM-Newton* satellite (Jansen et al. 2001) on 2002 October 7. The EPIC-MOS (Turner et al. 2001) and pn (Strüder et al. 2001) cameras were operating in Small Window Mode, observing through the Thin Filter. The Optical Monitor (OM; Mason et al. 2001) observed for 15 ks through the UVW1 filter and for 12 ks through the UVM2 filter. The RGS instruments collected 36 ks of data, however the count-rate was too low to allow for phase-resolved analysis, so these data are not presented in this paper.

We analysed the observation using the XMM-SAS software v6.0.0, extracting data from a circular region radius 20 arc sec. Only single- and double-pixel events were selected. The entire small window of the central CCD in the EPIC-MOS detectors was affected by source counts, so we used an adjacent chip to estimate the background. For the EPIC-pn camera, in which only the on-axis CCD is exposed in Small Window Mode, we used as much area as was free of source counts to estimate the background. Some times of high background were rejected, totalling 850 s in the MOS detectors

* pae@astro.keele.ac.uk

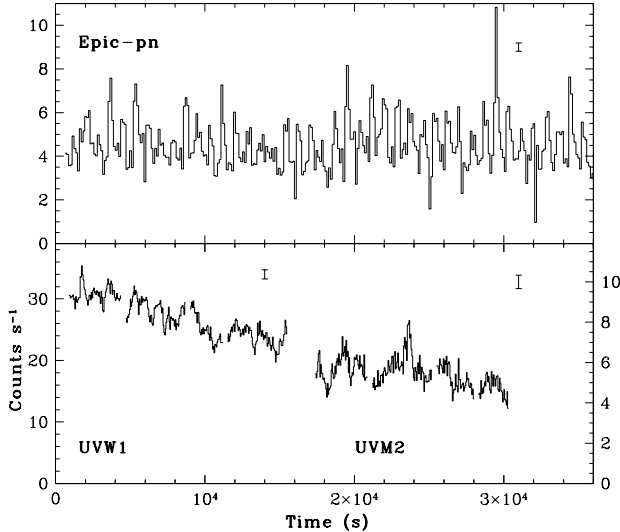


Figure 1. Top panel: the EPIC-pn X-ray lightcurve binned at 120 s. Lower panel: The UV lightcurves binned at 50 s (the UVW1 filter has a 2450–3200-Å bandpass and the UVM2 filter has a 2050–2450 Å bandpass). The prominent modulation is the 833-s spin period. Typical errors are shown.

and 550 in the pn. Lightcurves are shown in Fig. 1, and are dominated by modulation at the 833-s white-dwarf spin period. The EPIC-pn camera shows a mean count rate of 4.5 counts s⁻¹, which implies a 0.2–12 keV flux of 6×10^{-14} W m⁻².

Fourier transforms (Fig. 2), reveal spin-period modulation in both the X-ray and UV emission, but no power is seen at the beat frequency between the spin and orbital cycles. Power at the beat frequency is seen in the X-ray power spectra of some IPs and is thought to indicate a portion of the accretion stream overflowing the disc and coupling to the magnetosphere directly (e.g. FO Aqr, Hellier 1993). However, no previous X-ray observation of PQ Gem has revealed power at the beat period, so its absence in our data is not surprising.

3 EPHEMERIS

Mason (1997) showed that the white dwarf in PQ Gem is spinning down, and developed a quadratic ephemeris for the spin pulse. By the time of our observation, this has developed cycle count uncertainties, and thus we update it using *RXTE*, *ASCA* and *Chandra* X-ray observations from the HEASARC archives, and optical observations from the CBA archives (Kemp, private communication). For consistency with Mason (1997) we take the centroid of the soft X-ray dip as the phase zero point. This feature is less prominent in our data, however from previous work (e.g. Mason 1997) it can be well constrained as occurring 0.2 cycles before soft X-ray maximum. Also, on this phasing the hard X-ray dip occurs at phase 0.023, the *B*-band maximum at 0.154, *I*-band maximum at 0.433 and the *V*-band minimum occurs at phase 0.643 (Mason 1997; Hellier et al. 1994), allowing us to use all types of data if we assume that these relative phasings have not changed over the last ten years. The resultant timings, converted to TDB, are listed in Table 1.

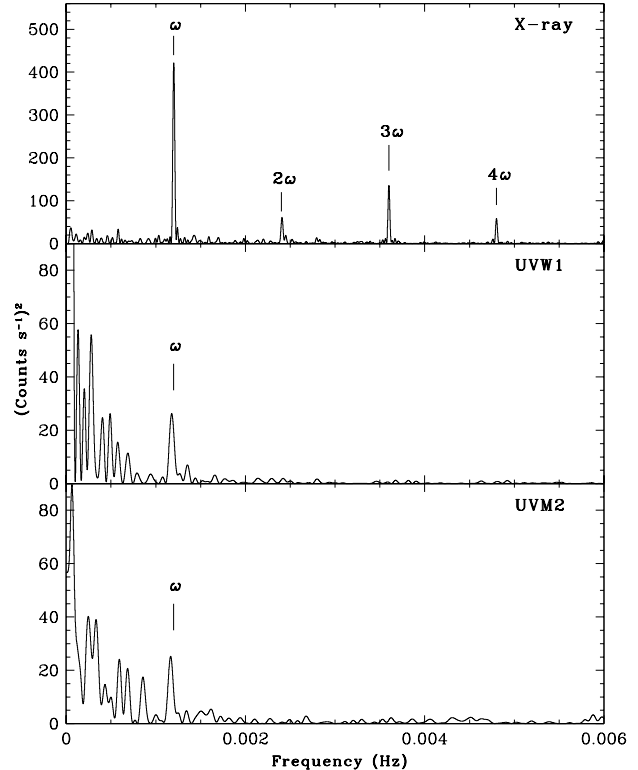


Figure 2. Power spectra of the X-ray (MOS+pn, upper panel) and UV (centre and lower panels) data. The spin frequency is denoted by ω . The low frequency peaks in the UV data are caused by flickering.

Band	Date	Duration (ks)	Cycle	TDB (-240 0000)
<i>RXTE</i>	1997-01-27	25.9	38620	50475.68457
Optical (<i>V</i>)	1998-02-11	6.7	78129	50856.79208
<i>ASCA</i>	1999-10-19	94.5	141826	51471.22305
<i>Chandra</i>	2000-04-09	52.3	159714	51643.77526
Optical (<i>B</i>)	2002-02-12	15.4	229678	52318.66493
Optical (<i>I</i>)	2002-02-19	22.1	230293	52324.59754
<i>XMM-Newton</i>	2002-10-07	35.7	254226	52555.46150
Optical (<i>B</i>)	2003-12-22	4.8	299997	52996.98217

Table 1. Timings of phase zero, as defined in the text.

The best-fitting quadratic ephemeris calculated is:

$$\text{TDB}_{\text{dip}} = 245\ 0103.152344(53) + 0.0096460639(4)N + 4.379(26) \times 10^{-13}N^2$$

and is shown in Fig. 3. Adding a cubic term had little effect on the quality of the fit and is thus not done. Note that this gives a slightly longer period than Mason (1997), and a smaller value for the period change.

4 SPECTROSCOPY

We extracted source and background spectra from the regions defined in Section 2, and used the XMM-SAS RMFGEN

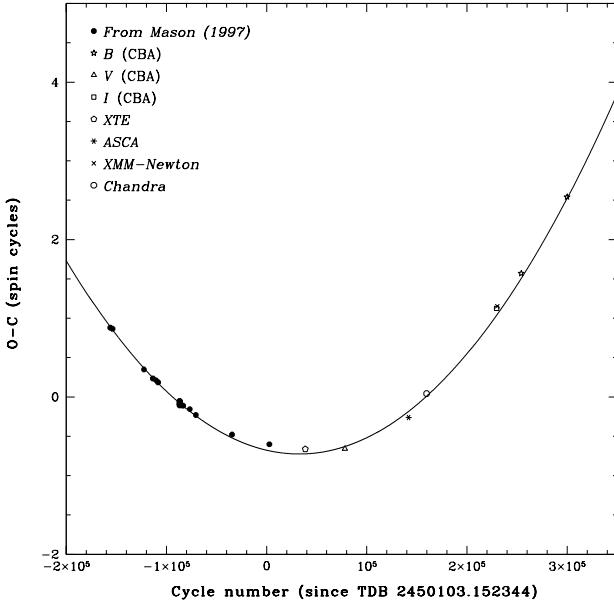


Figure 3. $O - C$ diagram of PQ Gem showing the data from Table 1 and the quadratic ephemeris given in Section 3.

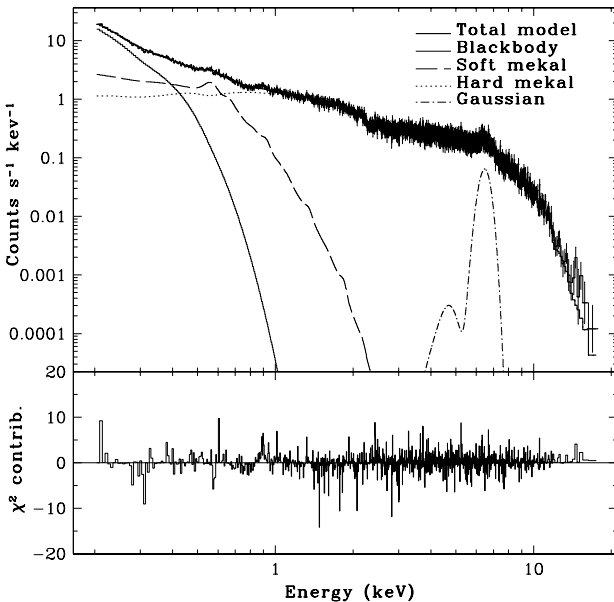


Figure 4. The phase-averaged spectrum with the fitted model and the contributions from each component shown.

and ARFGEN tasks to create the response matrices, for use in XSPEC. When fitting the spectra we allowed the emission normalisations to optimise independently for each instrument to minimise the effects of calibration uncertainties between detectors.

The X-ray emission in an IP arises from plasma heated to X-ray temperatures at a stand-off accretion shock, which then cools as it approaches the white-dwarf surface (e.g. Aizu 1973; Cropper et al. 1999). We thus initially fitted two MEKAL components with different temperatures but an identical abundance, absorbed by both simple and partial covering absorption. This gave a best-fitting χ^2 of 3247

($\chi^2_{\nu}=1.33$). We did not add further MEKAL components, since the negligible χ^2 improvement did not justify the additional free parameters. An alternative model is the full column-fitting approach of Cropper et al. (1999), however we prefer a simple parameterisation of the data, allowing us to study spectral changes over the spin pulse with fewer assumptions about the accretion column structure.

Following previous studies (e.g. Mason et al. 1992; Duck et al. 1994; de Martino et al. 2004) we added a soft blackbody to our model, improving the fit to a χ^2 of 2887 ($\chi^2_{\nu}=1.18$). Since dense absorption will completely smother such soft emission, the blackbody was acted on only by a simple absorber, which was separate from that acting on the MEKALs.

There were still significant residuals at the 6.4-keV iron fluorescence line, so we added a narrow Gaussian; this further reduced χ^2 to 2719 ($\chi^2_{\nu}=1.12$). The fitted equivalent width (93.2 ± 19 eV) is comparable with that found in other IPs observed with *XMM* (FO Aqr: 129 eV, Evans et al. 2004; V405 Aur: 121 eV, Evans & Hellier 2004).

The resultant model is shown in Fig. 4 and Table 2. Note that some of these parameters may change on the spin period, and thus the values in the table will be weighted averages. We find a best-fitting blackbody temperature of 44 ± 9 eV, in good agreement with previous studies (Duck et al. 1994 found 46_{-23}^{+12} eV; de Martino et al. 2004 reported 56_{-14}^{+12} eV). The temperature of the hard MEKAL component was 39_{-6}^{+4} keV, which compares with 17 ± 2 keV from *BepoSAX* data (de Martino et al. 2004) and ~ 70 keV from *Ginga* data (Duck et al. 1994). The de Martino et al. value is likely to be most reliable, since the *BepoSAX* detection extends to harder energies (70 keV versus 12 keV in XMM data), but note that they fitted a single-temperature model to the entire spectrum, so our results are not directly comparable.

Our fitted MEKAL abundance is $0.028 (\pm 0.004)$, which is very low and reflects the fact that the observed lines are much weaker than expected for the 0.2-keV component included in our model (at the temperature of the hotter component the plasma is almost entirely ionised, so this component has much less effect on the abundance than the cooler MEKAL). Note that this does not necessarily indicate a genuinely low metal abundance, but is probably caused by high opacity in the accretion columns, which will suppress line emission. de Martino et al. (2004) found a higher abundance of $0.33_{-0.09}^{+0.07}$, because they did not include a low-temperature MEKAL in their model. For comparison with de Martino et al., we tried removing the softer MEKAL component from our model, however this caused χ^2 to increase by ~ 1200 .

XSPEC also provides a CEMEKL emission model, which reproduces MEKAL emission along a continuous distribution of temperatures, with emissivity varying according to $(T/T_{\max})^{\alpha}$. Exchanging the two single-temperature MEKALs for a CEMEKL caused a very large (~ 800) increase in χ^2 , suggesting that emissivity in the accretion column does not have a power-law dependence on temperature.

5 PHASE-RESOLVED SPECTROSCOPY

We present spin-folded light-curves and a softness ratio in Fig. 5. In previously reported *ROSAT* data (Mason 1997),

Component	Parameter (Units)	Value	Error
Absn.	n_H (cm $^{-2}$)	4.75×10^{19}	(+1.74, -2.02)
	kT (eV)	43.9	(+8.7, -8.2)
Blackbody	Norm (pn)	2.44×10^{-4}	(+0.34, -0.35)
	n_H (cm $^{-2}$)	9.67×10^{20}	(+1.26, -1.95)
Absn.	n_H (cm $^{-2}$)	11.1×10^{22}	(+0.88, -0.73)
	CvrFract	0.450	(+0.006, -0.008)
Partial	Energy (keV)	6.40	frozen
	Norm (pn)	2.43×10^{-5}	(+0.42, -0.41)
Gaussian	Eq. Wid (pn, eV)	93.2	(+17.8 -17.5)
	kT (keV)	0.179	(±0.002)
Mekal	Abundance	2.82×10^{-2}	(+0.58, -0.20)
	Norm (pn)	5.84×10^{-2}	(+1.45, -1.29)
Mekal	kT (keV)	39.4	(+4.1, -6.3)
	Norm (pn)	1.77×10^{-2}	(+0.04, -0.03)

Table 2. Model components and parameters fitted to the phase-averaged spectrum (see Section 4). The errors, which are quoted to the same power of ten as the corresponding value are the 90% confidence errors according to formal statistics; note however that these are likely underestimates, since they do not account for the calibration systematics.

the soft X-rays show a dip at phase 0, a broad maximum centred on phase 0.2 and a ‘shoulder’ around phases 0.4–0.5. The harder X-rays show the dip and also a ‘spike’ coincident with the soft shoulder. Our data are similar, except that the X-ray dip is shallower. This was most prominent in *ROSAT* data (from 1993; Mason 1997), less so in *BeppoSAX* data (from 1996; de Martino et al. 2004), and still less prominent in our *XMM* data (from 2002).

To investigate these spectral changes we applied two models to four phase regions (the dip, the spike, and phases 0.2–0.4 and 0.6–0.9), testing whether the changes are reproduced by variations in absorption, model normalisation, or both. The first model was that developed in Section 4, in which the MEKAL temperatures and normalisations can vary with respect to one-another. The second model was the stratified column model of Cropper et al. (1999), which uses multiple MEKALS with temperatures and relative normalisations determined by the physics of an accretion column.

Both models gave adequate fits if both their normalisations and the absorption are allowed to vary on the spin cycle. An example fit is given in Table 3. Neither model gave an acceptable fit if only the absorption was allowed to change (with $\Delta\chi^2 \gtrsim 40$ when this was attempted, compared to a fit where all parameters can vary). We then tried instead forcing the absorption to remain constant across the spin cycle. The stratified column model did not give an acceptable fit in this case, however the greater freedom of the unconstrained MEKAL model did allow acceptable fits (χ^2 poorer by no more than 20) except during the dip. If we accept that the relative MEKAL normalisations must be constrained as in the stratified column model, this implies that the absorption must be allowed to vary between phase regions.

6 DISCUSSION

Potter et al. (1997) and Mason (1997) developed a model for PQ Gem based on optical photometry, polarimetry and

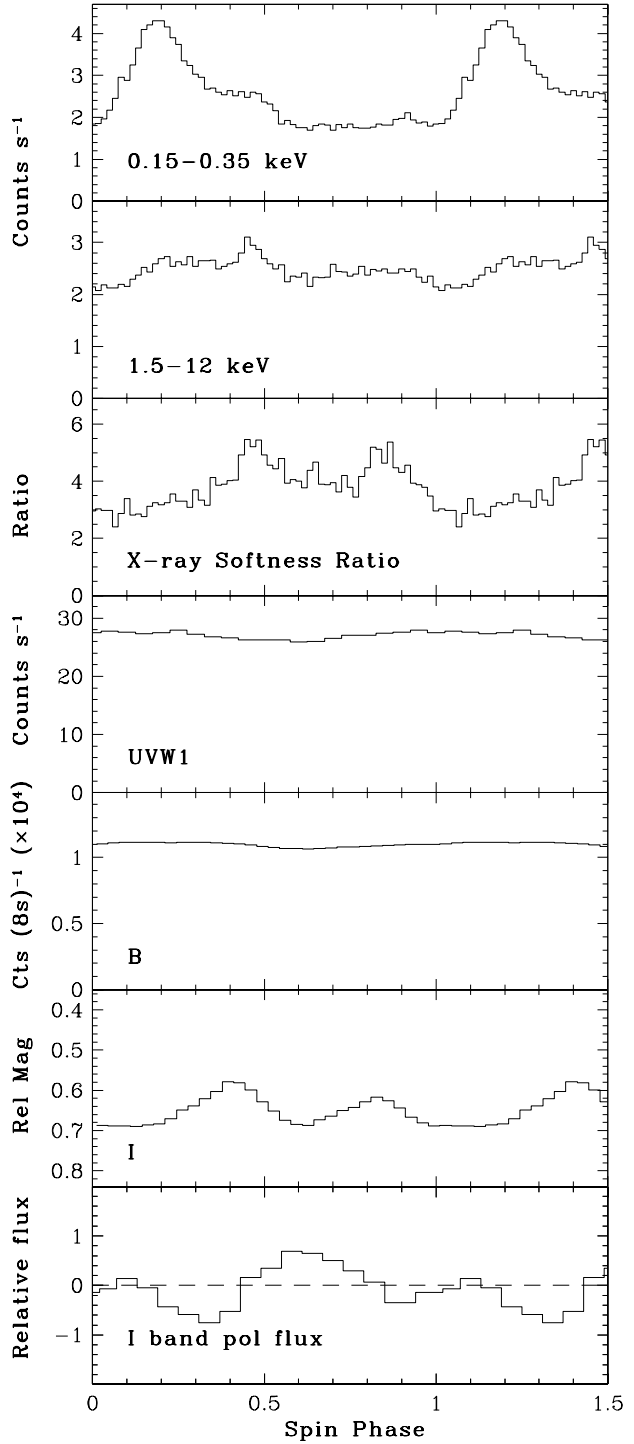


Figure 5. Spin folds of PQ Gem. The upper two panels show the soft and hard X-ray folds. The softness ratio is defined as (1.5–4)/(6–12) keV. The *B* and *I* band data are taken from Hellier et al. (1994), and the polarised flux is found from the *I* band flux in Hellier et al. (1994) and the polarimetry of Potter et al. (1997). Phase zero corresponds to the X-ray dip, as in our ephemeris (Section 3).

Parameter (units)	Dip		Spike	
Phase region	0.95–1.05	0.2–0.4	0.4–0.5	0.6–0.9
Abs n_{H} (10^{19} cm $^{-2}$)	16.0 (+23.6, -8.01)	2.4 (+6.2, -2.4)	7.1 (+14.1, -7.1)	13.3 (+13.1, -5.2)
B-body kT (eV)	37.4 (+1.9, -7.4)	45.9 (+3.2, -3.4)	41.5 (+2.5, -6.6)	39.8 (+5.2, -5.6)
Norm (pn $\times 10^{-4}$)	4.2 (+21.7, -2.32)	3.1 (+1.7, -2.5)	3.0 (+3.3, -1.3)	2.8 (+3.5, -1.4)
Abs n_{H} (10^{21} cm $^{-2}$)	0.86 (+0.29, -0.19)	1.16 (+0.20, -0.26)	0.91 (+0.22, -0.30)	1.05 (+0.24, -0.29)
PCF n_{H} (10^{22} cm $^{-2}$)	8.2 (+2.1, -1.7)	12.7 (+2.2, -2.0)	9.4 (+3.2, -2.2)	12.7 (+2.5, -2.2)
CvrFract	0.526 (+0.032, -0.030)	0.529 (+0.032, -0.026)	0.343 (+0.044, -0.021)	0.393 (+0.039, -0.031)
Mekal kT (eV)		177 \pm 3, tied across all regions		
Abundance ($\times 10^{-2}$)		2.40 (+0.53, -0.49), tied across all regions		
Norm (pn $\times 10^{-2}$)	6.74 (+0.37, -0.34)	8.70 (+0.34, -0.38)	7.23 (+0.36, -0.34)	6.83 (+0.26, -0.25)
Mekal kT (keV)		38.7 (+8.5, -8.0), tied across all regions		
Norm (pn $\times 10^{-2}$)	1.615 (+0.088, -0.0082)	2.083 (+0.081, -0.092)	1.731 (+0.087, -0.081)	1.634 (+0.061, -0.059)

Table 3. The model parameters when the four phase regions are fitted simultaneously, with absorption and normalisation free to vary. The MEKAL temperatures and abundance were tied between regions, as was the ratio of their emission normalisations.

X-ray observations. In this model the accreting field lines at the upper magnetic pole lie in our line of sight at phase zero, obscuring our view of the X-ray emitting accretion footprints and causing the X-ray dip. However, to explain asymmetries in the lightcurve, the accretion needs to be predominantly along field lines preceding the pole; thus the magnetic pole itself is not on the white-dwarf meridian until phase 0.1.

By phase 0.1 the curtains are moving out of our line of sight, so the X-ray and UV flux start to rise (Fig. 6). By phase 0.2 the accretion curtains have moved on, giving us a relatively unobscured view of the heated white-dwarf surface near the accretion column. This results in soft-X-ray maximum.

While the soft X-ray emission comes from the heated white-dwarf surface, the I -band flux comes from cyclotron emission in the accretion columns above the surface. We see maximum I -band flux when the magnetic poles are across our line of sight, and we can see emission from both poles simultaneously (e.g. phase 0.4, see Figs. 5 and 6). I -band minima occur when the magnetic axis points towards us and we see only one pole.

6.1 Implications of our data

In Section 5 we concluded that the absorption varies over the spin cycle. This can be explained by the accretion curtain model, in which opacity along the line of sight is highest when the curtain points towards us (phase 0 in Fig 6) and lowest half a cycle later (phase 0.5), producing a sinusoidal variation in the softness ratio (see, e.g., Hellier, Cropper & Mason 1991, and the modelling by Kim & Beuermann 1995).

The overall softness variation in Fig. 5 has the correct phasing to be explained as above, however there is a reduction in softness during phases 0.5–0.8, giving apparent maxima at phases 0.45 and 0.85. We suggest that this could arise if the base of the upper accretion column has passed over the white-dwarf limb (see Fig. 6) such that we don't see the softest emission from the cooler regions near the base

of the column. To complete the explanation we would also need an asymmetry between the upper and lower poles so that the base of the lower pole did not appear and produce an opposite effect; alternatively, if there were considerable opacity in the orbital plane, it could prevent soft emission at the lower pole being seen.

In the hard X-ray pulse profile we see a 'spike' at phases 0.4–0.5, coincident with a 'shoulder' in the soft X-ray decline. Mason (1997) suggested that the lower accretion region could be larger than the upper one, thus at phases 0.4–0.5 we could be seeing both columns and footprints, explaining these features. We also note that the softness rises during phases 0.2–0.4, while the flux remains approximately constant, for which we do not have an explanation.

Turning to other wavelengths: the UV emission could arise from both the heated white-dwarf surface and the X-ray irradiated accretion curtains. In principle, more flux could be visible when the upper footprint points towards us, however this is countered by obscuration of this region by the accretion curtains (see Fig. 6), and the combination of these effects could explain the relatively low pulse fraction of ~ 7 per cent (Fig. 5).

However, since we do see more flux at phases 0.9–0.3 (Fig. 7), it is possible that some of the upper heated polecap is visible above the sweep of the curtain (see, e.g., the phase 0 panel of Fig. 6), as we have already argued to explain the soft X-ray lightcurve.

The pulsed B -band light can arise from a combination of the heated white dwarf, the accretion curtains, and the irradiated disc. The pulse has a depth of only ~ 4 per cent (Fig. 5), which suggests these components act in anti-phase.

6.2 Field-disc interaction

The fact that the white dwarf in PQ Gem is spinning down (Section 3) implies that it is not in equilibrium. Further, Mason (1997) suggests that the accreting field lines thread the accretion disc a little outside the corotation radius, so

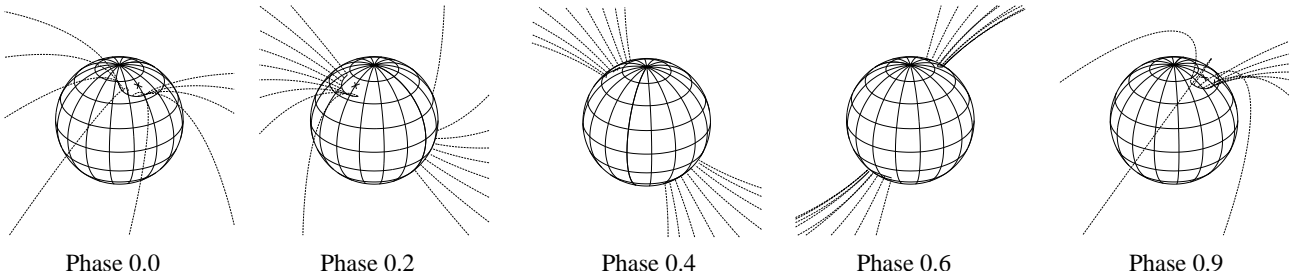


Figure 6. Schematic diagrams during the X-ray dip (phase 0.0), blackbody maximum (phase 0.2), the ‘spike’ (phase 0.4), phase 0.6, and phase 0.9.

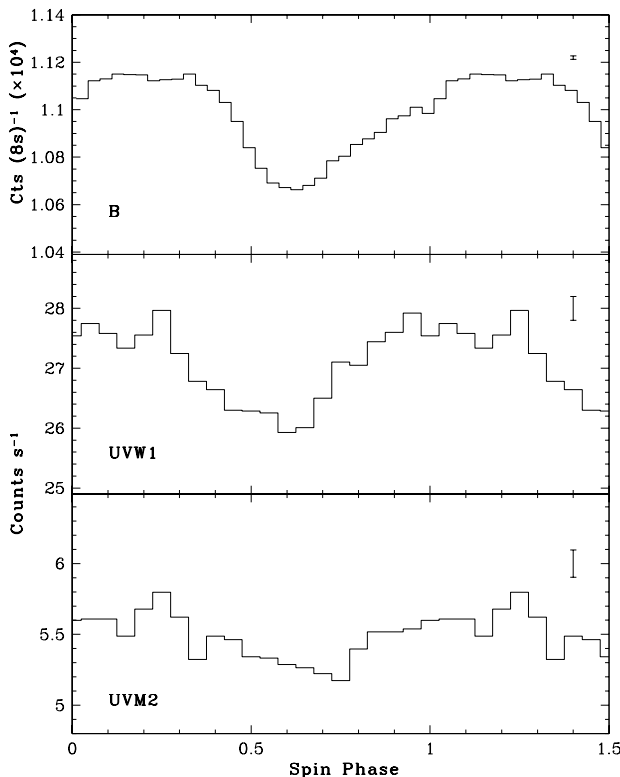


Figure 7. The pulse-profile of PQ Gem in the UV and *B* bands. The scale here has been enlarged to show the shape of the pulses. Typical photon-noise errors are shown, though uncertainties owing to flickering are likely to be larger (see Fig. 2).

that the slower-moving disc material exerts a spin-down torque on the dipole. We would then expect the field lines to be swept backwards, particularly near the threading region where magnetic and material pressures are roughly balanced. As discussed by Mason (1997), it is hard to see how a field line that is swept back and moving faster than the local disc can scoop up material. However, a field line ahead of the pole will meet the disc at an inclined angle that counteracts any effect of being swept back. Thus accreting along leading field lines may be a consequence of the fact that the white dwarf is spinning faster than equilibrium.

Testing such ideas by applying them to other IPs is hampered by the fact that in few systems do the spin-pulse lightcurves give sufficient observational clues for us to deduce the layout of the accreting field lines. However,

in FO Aqr we found that the accretion is predominantly along field lines swept back from the magnetic pole (e.g. Evans et al. 2004). This lag, however, appears to persist both when the white dwarf is spinning up and when it is spinning down, which argues against any simplistic interpretation. Thus, study of intermediate polars is giving us observational clues to the difficult topic of how a magnetic field interacts with an accretion disc, but study of a greater sample of systems is needed to make further progress.

ACKNOWLEDGEMENTS

This research has made use of data obtained through the High Energy Astrophysics Science Archive Research Center Online Service, provided by the NASA/Goddard Space Flight Center. We also thank Jonathan Kemp and Joe Patterson for providing us with optical photometry of PQ Gem from the CBA archives. The *XMM-Newton* observations were obtained as part of the Optical Monitor Guaranteed Time programme.

REFERENCES

- Aizu K., 1973, *Prog. Theor. Phys.*, 49, 1184
- Cropper M., Wu K., Ramsay G., Kocabiyik A., 1999, *MNRAS*, 306, 684
- de Martino D., Matt G., Belloni T., Haberl F., Mukai K., 2004, *A&A*, 415, 1009
- Duck S.R., Rosen S.R., Ponman T.J., Norton A.J., Watson M.G., Mason K.O., 1994, *MNRAS*, 271, 372
- Evans P.A., Hellier C., 2004, *MNRAS*, 353, 447
- Evans P.A., Hellier C., Ramsay G., Cropper M., 2004, *MNRAS*, 349, 715
- Hellier C., 1993, *MNRAS*, 265, L35
- Hellier C., 1997, *MNRAS*, 288, 817
- Hellier C., 2001, *Cataclysmic Variable Stars*, Springer-Praxis, Chichester, UK
- Hellier C., Cropper M., Mason K.O., 1991, *MNRAS*, 249, 235
- Hellier C., Ramseyer T.F., Jablonski F.J., 1994, *MNRAS*, 271, L25
- Jansen F. et al., 2001, *A&A*, 365, L1
- Kim, Y., Beuermann K., 1995, *A&A*, 298, 165
- Mason K.O., 1997, *MNRAS*, 285, 493
- Mason K.O. et al., 1992, *MNRAS*, 258, 749
- Mason K.O. et al., 2001, *A&A*, 365, L36
- Patterson J., 1994, *PASP*, 106, 209
- Pirola V., Hakala P., Coyne G.V., 1993, *ApJ*, 410, L107
- Potter S.B., Cropper M., Mason K.O., Hough J.H., Bailey J.A., 1997, *MNRAS*, 285, 82

Strüder L. et al., 2001, A&A, 365, L18
Turner M.J.L. et al., 2001, A&A, 365, L27